Dalton Transactions

Accepted Manuscript

ROYAL SOCIETY OF CHEMISTRY

www.rsc.org/dalton

Journal Name

ARTICLE

A Vacuum-annealing Strategy for Improving Near-infrared Super Long Persistent Luminescence in Cr^{3+} Doped Zinc Gallogermanate Nanoparticles for Bio-imaging

Received 00th January 20xx,
Accepted 00th January 20xx

DOI: 10.1039/x0xx00000x

www.rsc.org/

Jian Yang,[a] Yuxue Liu,[*a,b] Duanting Yan,[a] Hancheng Zhu,[a] Chunguang Liu,[a] Changshan Xu,[a] Li Ma,[b] Xiaojun Wang[*a,b]

Novel Cr^{3+} doped zinc gallogermanate (ZGGO) nanoparticles with 697 nm near-infrared (NIR) super long afterglow were prepared by hydrothermal method. Subsequently, a vacuum-annealing strategy was adopted to improve NIR afterglow in ZGGO:Cr^{3+} nanoparticles. For the sample annealed at 800 °C, no variation in the particle size is observed, the persistent luminescence increases by an order of magnitude (~ 14 times) and NIR afterglow time reaches to more than 15 hours relative to the as-prepared sample. After the annealing at temperatures higher than 880 °C, the persistent luminescence of the nanoparticles is enhanced, but they show aggregated-surface behavior. Meanwhile there generates the shallow and deep traps, related to Zn_{Ga}'-Ga_{Zn}^{o} antisite defects and V_{Ge}-Cr^{3+}-V_O defect clusters, respectively. Finally, we apply ZGGO:Cr^{3+} persistent luminescence nanoparticles (PLNPS) to human serum albumin (HSA) colloid solution, more than 1 h NIR persistent luminescence is detected under 320 nm excitation. The quenching effect of NIR luminescence by OH^- in HSA solution is observed based on the reduced contribution of surface Cr^{3+} in PLNPS to NIR luminescence. Our results suggest that ZGGO:Cr^{3+} PLNPS have potential applications for in vivo bio-imaging.

Introduction

Recently, near infrared (NIR) super long persistent luminescence nanoparticles(PLNPS) are of interest due to the unique advantages, such as no auto-fluorescence effect of the tissue and high revolution imaging with deep penetration, as a tool for *in vivo* imaging and diagnosis applications in living animal. [1-8] *In vivo* imaging with $Ca_{0.2}Zn_{0.9}Mg_{0.9}Si_2O_6$:$Eu^{2+}$, Mn^{2+}, Dy^{3+} and $CaMgSi_2O_6$:Eu^{2+}, Mn^{2+}, Pr^{3+} PLNPS (the particle size of 100 nm) in mice were realized, but the real-time monitoring was merely in the range of 15-120 min reported by Scherman et al.[2, 3]

To further improve persistent luminescence, novel Cr^{3+} doped zinc gallogermanate (ZGGO) persistent phosphors, such as $Zn_3Ga_2Ge_2O_{10}$:Cr^{3+} ceramic disc and $ZnGa_2O_4$:Cr^{3+},Ge/Sn powders were prepared by a solid state method and the longest afterglow time was reported to be 360 hours.[4, 9] This super long persistent luminescence may relate to the existence of Ge in the material and might be originated from the formation of V_{Ge}-Cr^{3+}-V_O defect clusters.[4]

More recently, the synthesis of ZGGO:Cr^{3+} nanoparticles by citrate sol-gel method in combination with a subsequent calcination in air was reported and the *in vivo* imaging could be monitored for more than 15 hours in mice after subcutaneous injection.[10] For different kinds of PLNPS, few research on a subsequent thermal annealing process to obtain intense NIR luminescence was performed. At present, to what degree the thermal annealing improves PLNPS long persistent luminescence and how it affects the particle size and defect traps are still unclear. On the other hand, it is essential to unravel the contributions of interior and surface luminescent centers in PLNPS to the NIR luminescence. The understanding is helpful for different kinds of nanoparticles to further improve the persistent luminescence and expand their medical applications.

In this work, ZGGO:Cr^{3+} PLNPS with the averaged particle size of 82 nm and 697 nm near-infrared persistent luminescence were prepared by a one-step hydrothermal synthesis route. Subsequently, a vacuum-annealing strategy is adopted to improve NIR afterglow in ZGGO:Cr^{3+} nanoparticles. For the sample annealed at 800 °C, the persistent luminescence intensity increases by nearly ~14 times relative to the as-prepared sample while the particle size remains nearly the same. For the annealed ZGGO:Cr^{3+} at 880 and 950 °C, the particle size exhibits an increase and the deep traps related with Zn, Ga and O vacancies dominates the persistent luminescence. In addition, the contributions of surface and interior Cr^{3+} in ZGGO PLNPS to the persistent luminescence were studied using luminescence kinetic analysis. Finally, for the ZGGO:Cr^{3+} PLNPS dispersed in human serum albumin(HSA)

[a.] School of Physics, Northeast Normal University, 5268 Renmin Street, Changchun 130024, China. E-mail: yxliu@nenu.edu.cn; Fax: +86-0431-85099851; Tel: +86-0431-85099851
[b.] Department of Physics, Georgia Southern University, Statesboro, GA 30460. E-mail: xwang@georgiasouthern.edu; Fax: +1-912-478-0471; Tel: +1-912-478-5503
.

solution, more than 1 h NIR persistent luminescence was recorded. It suggests that ZGGO:Cr^{3+} PLNPS have potential applications for *in vivo* bio-imaging.

Experimental

Synthesis and Characterization.

Cr^{3+} doped zinc gallogermanate Nanoparticles were prepared by hydrothermal method. Gallium (III) nitrate hydrate ($Ga(NO_3)_3 \cdot xH_2O$, 99.9%)(Sigma-Aldrich), germanium (IV) chloride ($GeCl_4$, 99.99%) (Sigma-Aldrich), zinc acetate ($Zn(CH_3COO)_2$, 99.99%) (Aladdin) and chromium (III) nitrate nonahydrate ($Cr(NO_3)_3 \cdot 9H_2O$, 99.95%) (Aladdin) as starting materials were dissolved in deionized water according to the proposed metal mole ratio in $Zn_2Ga_{2.98}Ge_{0.75}O_8:Cr^{3+}{}_{0.02}$ (ZGGO:Cr^{3+}). Then the solution was heated at 180 °C for 24 h in a Teflon-line steel autoclave with a capacity 40 ml. Precipitates appeared when it was cooled down to room temperature. Subsequently, the Precipitates was washed with deionized water three times and then dried at 80 °C for 4 h to obtain as-prepared ZGGO:Cr^{3+} PLNPS. The as-prepared PLNPS were collected and annealed at 800, 880 and 950 °C in a vacuum furnace with the pressure of 2.3×10^{-3} Pa for 1.5 h, respectively.

The crystal structures of the ZGGO:Cr^{3+} PLNPS were examined by a Rigaku D/MAX-2500 X-ray diffraction (XRD) spectrometer using Cu Kα radiation (0.15418 nm) over the angular range 10 to 80 degrees. The sample microstructures were investigated by means of a scanning electron microscope (SEM, FEI, Quanta FEG 250). The emission and excitation spectra were recorded with a SHIMADZU RF-5301PC spectrophotometer and a Zolix Omin λ-300 spectrophotometer with a R928 photomultiplier tube. The luminescence decays were taken with a LeCroy digital oscilloscope(62MXs-B), a Zolix Omin λ-300 spectrophotometer, a INNOLAS laser(SpitLight 600) and an INNOLAS optical parametric oscillator. Persistent luminescent decay measurements were carried out by using SHIMADZU RF-5301PC spectrophotometer and Zolix Omin λ-300 spectrophotometer. ZGGO:Cr^{3+} PLNP samples were pressed into pellets with a diameter of 13 mm to measure TSL spectra monitored at 697 nm from 88 to 673 K using RF-5301PC spectrophotometer and a Linkam THSM600/TMS94 stages. The heating rate was 5 K/min. The energy dispersive spectroscopy (EDS) was collected using Field Emission Transmission Electron Microscope (TEM, JEOL-2100F).

Imaging. All the digital photographs of the ZGGO:Cr^{3+} pellets and the nanoparticles dispersed solution (ZGGO:Cr^{3+} PLNPS annealed at 800 °C dispersed in 5% HSA solution at a concentration of 5 mg/mL) were carried out using a Digital Single Lens Reflex camera.

Results and discussion

The XRD patterns of the as-prepared and the annealed ZGGO:Cr^{3+} at 800, 880 and 950 °C are shown in Fig. 1. All

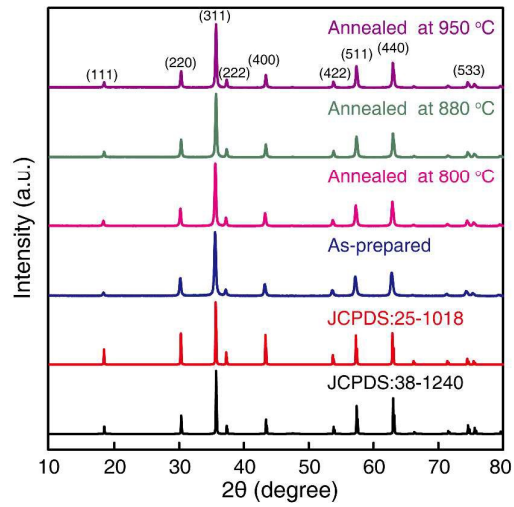

Fig. 1 XRD patterns of the as-prepared and the annealed ZGGO:Cr^{3+} samples at different temperatures.

diffraction peaks can be attributed to $ZnGa_2O_4$ (JCPDS: 38-1240) or Zn2GeO4 (JCPDS: 25-1018). The peak intensity ratios of (222) plane/(311) plane ($I_{(222)}/I_{(311)}$) are calculated and presented in Table 1. The ratios of the as-prepared and the annealed ZGGO:Cr^{3+} were in the range of 0.10-0.13 that is close to that of $ZnGa_2O_4$ (0.13), but smaller than that of Zn_2GeO_4 (0.20).

No impurity XRD peaks such as Zn, Ga_2O_3, ZnO, GeO_2 are detected. Since the radii of Zn^{2+}, Ga^{3+}, Cr^{3+} and Ge^{4+} ions are 0.60, 0.62, 0.615 and 0.54 Å, respectively, Cr^{3+} and Ge^{4+} ions might substitute for Ga^{3+} ions located at octahedral sites in $ZnGa_2O_4$ spinel structure.[9, 11, 12] For the samples annealed at 880 and 950 °C, the full width at half maximum (FWHM) of the (311) diffraction peak gives an obvious decrease as shown in Table 1. It can be attributed to the increase of the particle size and the crystallinity.[13]

Table 1 Dependence of XRD parameters of ZGGO:Cr^{3+} on the annealing temperature.

Annealing temperature	FWHM (degree)	$I_{(222)}/I_{(311)}$
As-prepared	0.292	0.103
800 °C	0.284	0.132
880 °C	0.251	0.132
950 °C	0.242	0.127
$ZnGa_2O_4$ (JCPDS:38-1240)	-	0.130
Zn_2GeO_4 (JCPDS:25-1018)	-	0.200

The SEM morphologies of the ZGGO:Cr^{3+} PLNPS with varying annealing temperature are shown in Fig. 2. It can be observed that the annealed nanoparticles at 880 and 950 °C exhibit aggregated surface. However, the annealed sample at 800 °C shows non-aggregated surface and an particle size of ~82 nm, which are similar to that of the as-prepared ZGGO:Cr^{3+}. These observations are in good agreement with XRD results.

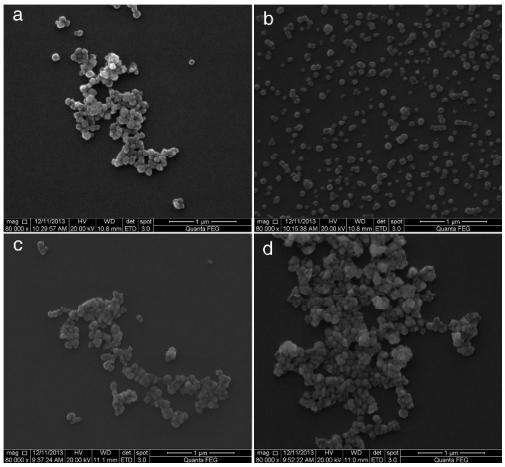

Fig. 2 SEM photographs of the as-prepared (a) and the annealed samples at 800 (b), 880 (c) and 950 °C (d).

The normalized excitation and emission spectra of the as-prepared and the annealed ZGGO:Cr^{3+} phosphors are presented in Fig. 3. The excitation spectrum of the as-prepared sample monitored at 697 nm covers a very broad spectral region from 220 to 660 nm. The 256 nm absorption can be ascribed to charge transfer band (CTB) from the octahedral O-Ga groups in the ZGGO:Cr^{3+} host.[6] The 320, 440 and 596 nm bands are attributed to the $^4A_2 \rightarrow {}^4T_1(^4P)$, $^4A_2 \rightarrow {}^4T_1(^4F)$ and $^4A_2 \rightarrow {}^4T_2(^4F)$ transitions, respectively.[4] Upon 596 nm excitation, the as-prepared sample exhibits an emission peak at 697 nm that superimposes on a broadband emission around 712 nm, which can be, respectively, assigned to the transitions from the ^2E and $^4T_2(^4F)$ levels to the $^4A_2$ ground-state level of Cr^{3+} occupying the distorted octahedral crystal field site.[4,14-17] For Cr^{3+} occupying strong-field sites, the ^2E state was lower than the $^4T_2$ level and the luminescence of Cr^{3+} ions is predominantly attributed to the $^2E \rightarrow {}^4A_2$ transition. Whereas, for Cr^{3+} occupying weak-field sites, the broadband $^4T_2(^4F) \rightarrow {}^4A_2$ transition is dominant.[18] The mixed emissions of 697 and 712 nm suggest the presence of Cr^{3+} ions locating at intermediate field sites where the crystal field strength is close to the crossing between the $^4T_2(^4F)$ and ^2E levels in the ZGGO:Cr^{3+} as shown in Fig. 3, which is similar to the case of $La_3Ga_5GeO_{14}$:Cr^{3+} phosphor.[19]

For the annealed samples, the excitation peak at 592 nm from the $^4A_2 \rightarrow {}^4T_2(^4F)$ transition exhibits a blue shift relative to that of the as-prepared sample (596 nm). In addition, FWHM of the emission around 712 nm becomes narrow and its intensity decreases. To explain the above results, the energy structure is given by the Tanabe–Sugano diagram (Fig. 4a).[20] When the strength of crystal field (Dq/B) is equal to 2.2, it is considered as the intermediate field case.[21, 22] When Dq/B>>2.2 or Dq/B<<2.2, Cr^{3+} ions locate at strong-field and weak-field sites, respectively. Grinberg et al. reported that the substitutionally disordered nature of gallogermanates creates a broad distribution of crystal-field strength and local disorder of the surrounding of the optical centers (Cr^{3+}) reduces the strength of the crystal field.[23] Here, for the annealed samples, the blue shift of the excitation peaks suggest that their $^4T_2$ level are higher than that of the as-prepared sample as shown in Fig. 4b. The higher $^4T_2$ level indicates that the number of Cr^{3+} locating at stronger field sites increases and the degree of local disorder decreases.[19, 24] Grinberg et al. also reported that the stronger substitutional disorder results in the inhomogenous broadening of both the $^2E \rightarrow {}^4A_2$ and $^4T_2(^4F) \rightarrow {}^4A_2$ transitions of Cr^{3+} ions in gallogermanate crystals, especially for $^4T_2(^4F) \rightarrow {}^4A_2$ transition.[18, 24, 25] Therefore, for the annealed samples, the narrower FWHM of the emission peaks indicates that the degree of the disorder of the

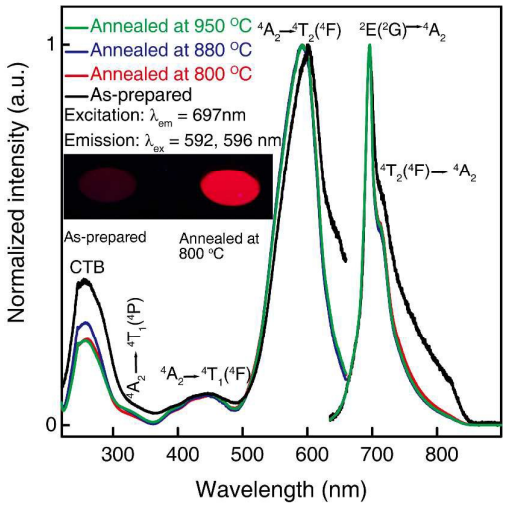

Fig. 3 Excitation (λ_{em} = 697 nm) and emission (λ_{ex} = 596 nm and λ_{ex} = 592 nm) spectra of the as-prepared and the annealed samples at different temperatures in vacuum for 1.5 hours. The inset shows the images of the as-prepared and annealed at 800 °C samples irradiated with UV light at 254 nm.

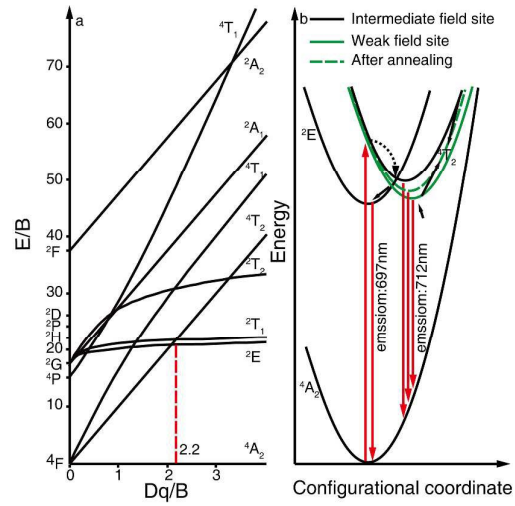

Fig. 4 (a) Tanabe–Sugano diagram representing the octahedrally coordinated $3d^3$ ion system. (b) Mechanistic configurational coordinate diagram illustrating different emission channels from the Cr^{3+} ions doped in the ZGGO. The black, green solid and green dashed lines represent that the configurational coordinates of Cr^{3+} ions locate in intermediate crystal field, weak crystal field (before annealed) and weak crystal field (after annealed), respectively.

nearest-neighbor cations surrounding Cr^{3+} ions decreases (the crystallinity increases) and the local symmetry of Cr^{3+} ions becomes higher after the annealing. Furthermore, after the vacuum annealing, brighter NIR photoluminescence is observed under UV 254 nm excitation, as shown in Fig. 3 inset. For the annealed samples, the enhanced NIR emissions are in agreement with the increase of the crystallinity, which will be discussed in detail later.

The afterglow decay curves of the as-prepared and the annealed samples monitored at 697 nm after stopping 320 nm UV light irradiation for 5 min are shown in Fig. 5a. It can be seen that the persistent luminescence intensity increases with

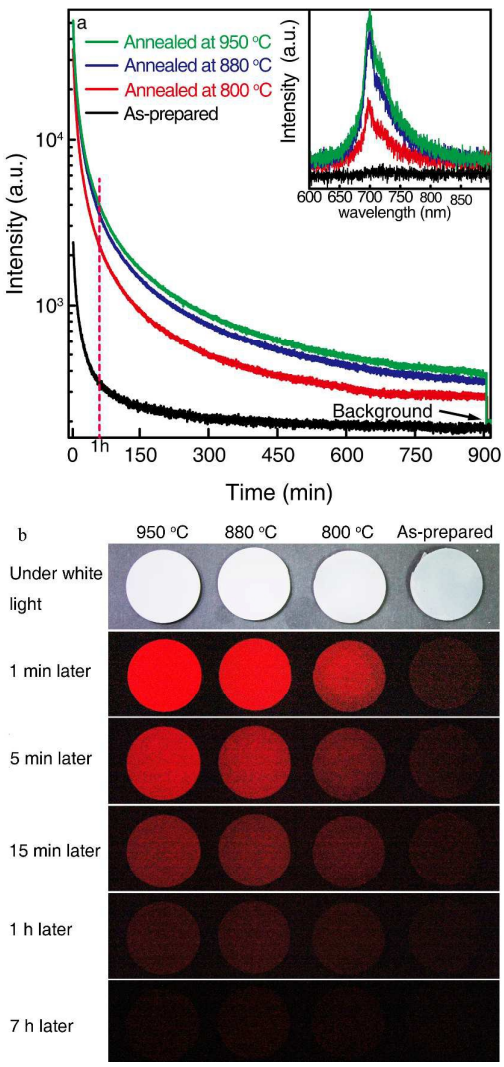

Fig. 5 (a) The afterglow decay curves of the as-prepared and the annealed samples monitored at 697 nm after turning off 320 nm UV light irradiation for 5 min. The upper inset shows four phosphorescence spectra recorded at 910 min after stopping the irradiation. (b) Images of four phosphor pellets under white fluorescent light (parameters: auto/ISO 400/exposure times 1/125s), the red digital photos of four phosphor pellets were taken at different afterglow times (1 min to 7 hours) after irradiation by 254 nm (parameters: manual/ISO 6400/exposure times 30 s).

increasing the annealing temperature. Especially, after 1 h of the afterglow decay time, the intensity of the annealed ZGGO:Cr^{3+} at 800 °C increases by ~14 times compared with that of the as-prepared sample. The persistent luminescence spectra of the annealed ZGGO:Cr^{3+} can be clearly detected after 15 h, while no persistent luminescence observed for the as-prepared sample, as shown in Fig. 5a inset. Fig. 5b shows the red digital photos of the as-prepared and the annealed ZGGO:Cr^{3+} at 800, 880 and 950 °C after a 5 W 254 nm lamp irradiation for 5 min. Clearly, the NIR afterglow emission of the annealed ZGGO:Cr^{3+} is brighter than that of the as-prepared sample and can be observed after 7 h.

Furthermore, to understand the dependence of persistent luminescence on excitation wavelength, the phosphorescence decay curves of the annealed ZGGO:Cr^{3+} at 800 °C after stopping 256, 320 and 440 nm irradiation are shown in Fig. 6. The 320 and 440 nm irradiation can be attributed to the direct excitation of Cr^{3+} from the $^4A_2 \rightarrow {}^4T_1$ (^4P), $^4T_1$ (^4F) transitions, respectively. Upon 256 nm excitation, the undoped ZGGO host exhibits a blue emission band at 480 nm (Fig. 6 inset) that overlaps with the excitation band from the $^4A_2 \rightarrow {}^4T_1(^4F)$ transition of Cr^{3+}. A persistent energy transfer from host to the Cr^{3+} ions takes place. The excitation of 256 nm band also originates from $^4A_2 \rightarrow {}^4T_1(^4P)$ transition.[26, 27] Thus the NIR persistent luminescence intensity under 256 nm irradiation is higher than that under 320 and 440 nm irradiation.

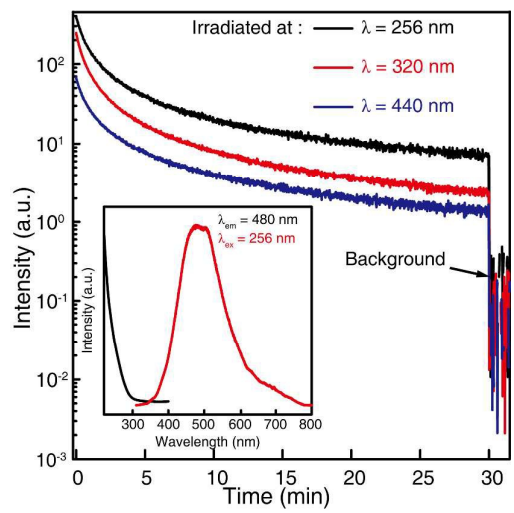

Fig. 6 The afterglow decay curves of the ZGGO:Cr^{3+} annealed at 800 °C after stopping the irradiation of 256, 320 and 440 nm UV light. The bottom inset shows excitation (λ_{em} = 480 nm) and emission (λ_{ex} = 256 nm) spectra of undoped ZGGO PLNPS annealed at 800 °C.

To unravel the contribution of the distribution of Cr^{3+} ions (interior and surface Cr^{3+} in nanoparticles) to the persistent luminescence, the luminescence decays of the Cr^{3+} emission monitored at 697 nm are measured as shown in Fig. 7. All the decays curves of Cr^{3+} need to be fitted with the sum of four exponentials and the fitting results are listed in Table 2. The two longer components (decay time in the order of ms) are attributed to the $^2E(^2G) \rightarrow {}^4A_2$ transitions of Cr^{3+} due to the forbidden spin-selection rule. The two shorter components (decay time in the order of μs) are contributed to the $^4T_2$ (^4F) → $^4A_2$ allowed transitions.[28] Generally, doped Cr^{3+} ions

in nanoparticles can be sorted into two different surroundings: surface and interior. The lifetime of the surface Cr^{3+} exhibits shorter decay time because of Cr^{3+} occupying low-symmetry sites. The lifetimes of interior and surface Cr^{3+} (τ_i and τ_S) from both $^2E(^2G) \rightarrow {}^4A_2(^4F)$ transition and $^4T_2(^4F) \rightarrow {}^4A_2(^4F)$ transition show an increasing trend with increasing the annealing temperature. It can be explained by the decreased non-radiative transition rate and the increased crystallinity after the thermal annealing.[29, 30] These results are consistent with the XRD analysis and SEM observation.

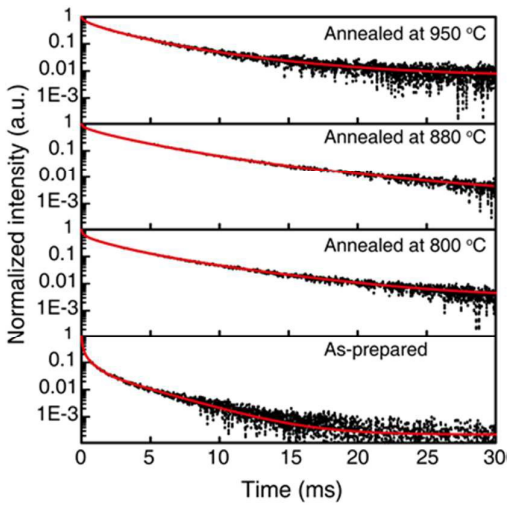

Fig. 7 Decay curves of Cr^{3+} in the as-prepared and the annealed ZGGO PLNPS at different temperatures. These curves all monitored at 697 nm and excited at 575 nm. The red line represents the fitting data using a four exponential function.

Table 2 The fitting parameters of Cr^{3+} emissions at 697 nm upon 575 nm excitation.

Annealing temperature	Decay [a] (μs) ($^4T_2 \rightarrow {}^4A_2$)	Decay [b] (ms) ($^2E \rightarrow {}^4A_2$)
As-prepared	τ_s = 21.2	τ_s = 0.62 (35%)
	τ_i = 121	τ_i = 2.97 (65%)
800 °C	τ_s = 32.0	τ_s = 2.07 (41 %)
	τ_i = 319	τ_i = 5.97 (59%)
880 °C	τ_s = 79.1	τ_s = 2.90 (49%)
	τ_i = 658	τ_i = 6.86 (51%)
950 °C	τ_s = 57.4	τ_s = 2.29 (47%)
	τ_i = 508	τ_i = 6.04 (53%)
HSA solution	τ_s = 30.9	τ_s = 1.99 (8%)
	τ_i = 311	τ_i = 5.99 (92%)

All samples are ZGGO:Cr^{3+} NPS: the as-prepared, the annealed at 800, 880 and 950 °C and HSA solution of ZGGO:Cr^{3+} PLNPS annealed at 800 °C. [a] Emission of $^4T_2 \rightarrow {}^4A_2$ transition of Cr^{3+}. [b] Emission of $^2E \rightarrow {}^4A_2$ transition of Cr^{3+}. τ_s: lifetime of surface Cr^{3+} in nanoparticles. τ_i: lifetime of interior Cr^{3+} in nanoparticles. The percentages in parentheses represent relative weights of luminescence from interior and surface Cr^{3+}.

Furthermore, for the as-prepared sample, based on the relative weight of Cr^{3+} emission ($^2E(^2G) \rightarrow {}^4A_2(^4F)$) from surface and interior Cr^{3+} in nanoparticles, the contributions of surface and interior Cr^{3+} to the NIR luminescence are 35% and 65%, respectively. For the annealed sample at 800 °C, the similar proportion (41% and 59%) can be obtained. It indicates that the vacuum-annealing at 800 °C does not give rise to redistribution of Cr^{3+} ions in nanoparticles. For the annealed samples at 880 and 950 °C, the increased proportion (49-47%) of the contribution of the NIR luminescence from surface Cr^{3+} can be observed, suggesting that more surface Cr^{3+} ions occupying low-symmetry sites are generated due to the formation of more defects in host after the thermal annealing at higher temperatures. Meanwhile, with increasing the annealing temperature, the increased Cr^{3+} ions on the surface might reduce the NIR luminescence due to surface effect such as lattice distortion and broken bond.[31] However, after the vacuum annealing, brighter photoluminescence is observed. The above results indicate that the variation in local environments around surface Cr^{3+} ions might have a contribution to the increased NIR luminescence after the annealing. It is consistent with the result that the thermal stability of the photoluminescence of Eu^{2+} with d-electron configuration in $CaAlSiN_3$:Eu^{2+}can be enhanced through a cation substitution strategy reported by Wang et al.[32]

The TSL glow curves of the as-prepared and the annealed ZGGO:Cr^{3+} are depicted in Fig. 8. It can be seen that the TSL

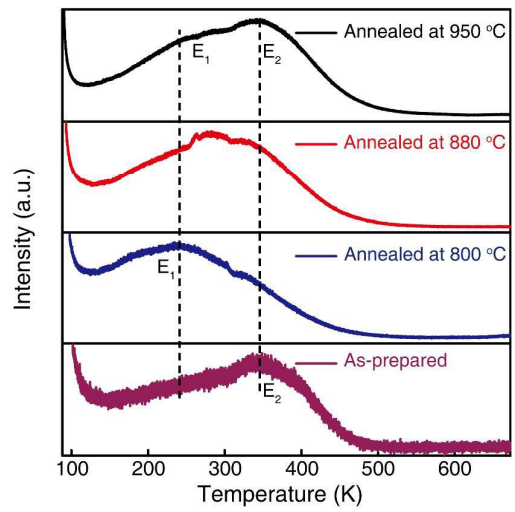

Fig. 8 TSL afterglow curves of the as-prepared and the annealed samples at 800, 880 and 950 °C measured after irradiation by 320 nm lights for 5 min. The heating rate is 5 K/min.

peaks show the broad and multiplet feature. The observed intense persistent luminescence in the low temperature region (<150 K) can be ascribed to the tunneling recombination process.[33] In 150-500 K regions, there exist two peaks around 240 and 340 K corresponding to shallow (E_1) and deep traps (E_2), respectively. E_1 and E_2 can be estimated using the expression $E \approx 25K_BT_M$ and the values are presented in Table 3.[26] For $ZnGa_2O_4$, Bessière et al. reported that TSL glow curve show a main peak at 318 K corresponding to deep traps and additional low-temperature peaks around 80, 145 and 205 K responsible for shallow traps. The deep and shallow traps can be attributed to Zn_{Ga}'-Ga_{Zn}^{o} antisite defects close to and far from Cr^{3+} ions, respectively.[6, 26, 34] For ZGGO:Cr^{3+}, the observed TSL peaks around 340 and 240 K might be associated with these antisite defects. Also, Pan et al. reported that the existence of Ge in ZGGO:Cr^{3+} can cause broader TSL peaks

compared with $ZnGa_2O_4$, suggesting new traps, such as V_{Ge}-Cr^{3+}-V_O defect clusters, are formed due to Ge doping.[4] After the vacuum-annealing, more shallow and deep traps are generated and the persistent luminescence is enhanced. For the annealed sample at 800 °C, the contribution from the shallow traps dominates TSL glow spectrum, while both traps comparably contribute to TSL signal for the samples annealed at 880 and 950 °C.

Table 3 Trap depth of the as-prepared and the annealed ZGGO:Cr^{3+} PLNPS at 800, 880 and 950 °C

Annealing temperature	Trap depth E (eV)	
	E_1	E_2
As-prepared	-	0.73
800 °C	0.52	0.70
880 °C	0.60	0.71
950 °C	0.62	0.73

To further elucidate the nature of the trap formation, mass loss rates of ZGGO:Cr^{3+} PLNPS as a function of the annealing temperature are illustrated in Fig. 9. Mass loss rate is defined as the ratio of the losing mass to initial mass. After annealed at 800 °C in vacuum, only 1% PLNPS is lost. With increasing the annealing temperature to 880-950 °C region, 6-9% of the mass is volatilized. EDX spectrum for the volatile substance attached to the wall of quartz tube furnace was obtained after annealed at 950 °C (inset, Fig. 9). The peaks associated with Zn, Ge and O atoms are observed (Cu and C related peaks in the spectrum come from the carbon-coated copper grid). It indicates that Zn, Ge and O atoms escape from ZGGO lattice and more vacancies, such as V_{Zn}, V_{Ge} and V_O, are generated in ZGGO lattice. It can be inferred that more Zn_{Ga}'-Ga_{Zn}^{o} antisite defects and V_{Ge}-Cr^{3+}-V_O defect clusters are formed. These results are consistent with the afterglow and TSL data.

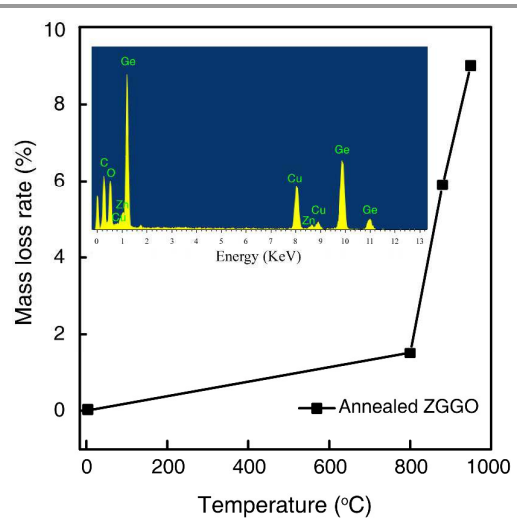

Fig. 9 Mass loss rates as a function of the annealing temperature. The inset shows the EDS spectrum of the volatile substance attached to the interior wall of the furnace after the annealing at 950 °C.

To understand the mechanism of NIR afterglow, the energy level diagram of Cr^{3+} ion in ZGGO:Cr^{3+} with respect to the conduction band (CB) and valence band (VB) and schematic representation of the NIR persistent luminescence is presented in Fig. 10. Upon 320 nm UV light excitation (or shorter wavelength), the ground-state electrons of Cr^{3+} ions are promoted to the $^4T_1$ (^4P) level and the excited electrons become the moving electrons in host through the thermal activation process.[4] The moving electrons are subsequently captured (process 1) and released (process 2) by the traps ($Trap_1$ and $Trap_2$). Meanwhile the tunneling processes (3 and 4) between $^4T_1$(^4F) state of Cr^{3+} and the traps ($Trap_1$ or $Trap_2$) occur. Under irradiation by 440 nm light, the persistent luminescence is mainly ascribed to the contribution from the tunneling process. Upon 256 nm UV excitation, there exist two processes: the energy transfer from host to Cr^{3+} (process 5) and the direction excitation of Cr^{3+} through $^4A_2 \rightarrow {}^4T_1$($^4P$) transition. Process 5 is involved in blue emission from ZGGO host. Thus, the ground-state electrons of Cr^{3+} ions are promoted to the $^4T_1$(^4P) or $^4T_1$(^4F) levels and NIR persistent luminescence is observed.

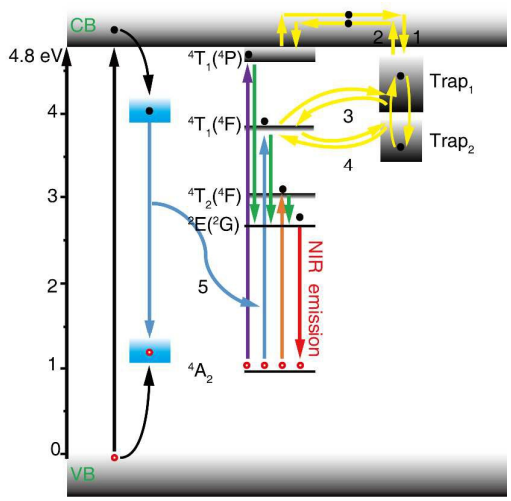

Fig. 10 Energy level diagram of Cr^{3+} ion in ZGGO is described with respect to the conduction band (CB) and valence band (VB) (energy band gap is about 4.8 eV) and schematic representation of the NIR persistent luminescence. 1, 2, 3 and 4 stand for the electron transfer processes. 5 represents the energy transfer from host to Cr^{3+} based on Ga-O group emission of ZGGO.

Since human serum albumin (HSA) acts as a major depot and transport protein, being capable of binding, transporting and delivering an extraordinarily diverse range of endogenous and exogenous compounds in the bloodstream to their target organs,[35] its solution can be used to simulate body fluids. We apply 15 mg ZGGO:Cr^{3+} PLNPS (annealed at 800 °C) to 3 ml colloidal solution with (HSA) 5% concentration and the aqueous dispersion can be obtained. Emission and excitation spectra of HSA aqueous dispersion is shown in Fig. 11. Upon 245 nm excitation, the intense broadband NIR emission with two peaks at 697 and 712 nm can be observed. From the excitation spectrum, the most efficient excitation for NIR emission is observed around 245 nm in UV region responsible for the O^{2-} (2p) to Ga^{3+}, Zn^{2+} (4s, 4p) CTB and the direct absorption of Cr^{3+}. For ZGGO:Cr^{3+} PLNPS powders, the most efficient excitation is located around 592 nm in the visible

region. The different behaviors indicate that the NIR luminescence under direct excitation of Cr^{3+} ions is drastically quenched by OH^- groups in HSA aqueous dispersion. Meanwhile, for ZGGO:Cr^{3+} in HSA solution, the 245 and 578 nm excitation peaks exhibit a blue shift relative to NPLPS powders (256 and 592 nm). According to Tanabe–Sugano diagram, it indicates that the number of Cr^{3+} located at stronger field sites are relatively increased in aqueous dispersion. It can be inferred that the luminescence from surface Cr^{3+} located at weak crystal field is quenched by the OH^- groups in HSA solution.[36-38]

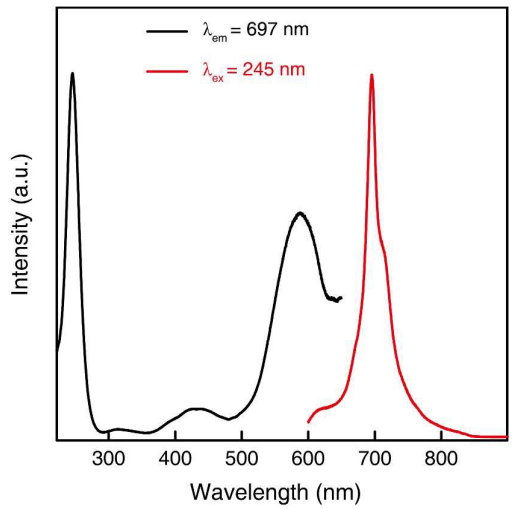

Fig. 11 Excitation and emission spectra of HSA aqueous dispersion of the annealed ZGGO:Cr^{3+} at 800 °C (5 mg/mL).

To further give an insight into the contributions of surface and interior Cr^{3+} ions in nanoparticles, a luminescence decay of Cr^{3+} emission monitored at 697 nm from ZGGO:Cr^{3+} dispersed in HSA solution is shown in Fig. 12 and the fitting results are

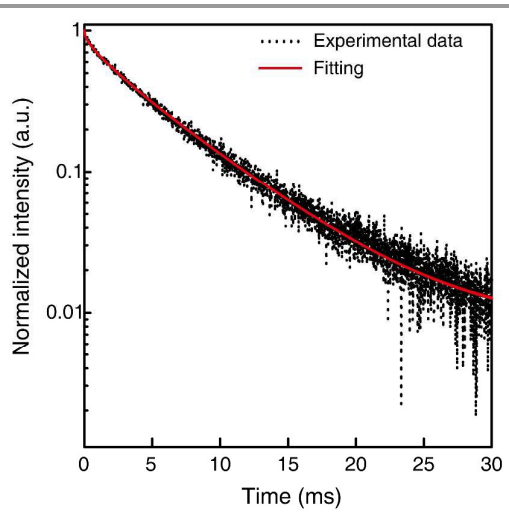

Fig. 12 Decay curve of Cr^{3+} in ZGGO:Cr^{3+} dispersed in HSA solution. The curve is monitored at 697 nm and excited at 575 nm. The red line represents the theoretical fitting using a four-exponential function.

listed in Table 2. It is found that the lifetimes of surface Cr^{3+} emission from both $^4T_2 \rightarrow {}^4A_2$ and $^2E \rightarrow {}^4A_2$ transitions exhibit a decrease compared with that of PLNPS due to the existence of the OH^- groups in HSA solution. The ratio of relative weight of the Cr^{3+} emission ($^2E(^2G) \rightarrow {}^4A_2(^4F)$) from surface to that from interior Cr^{3+} in HSA solution is about 0.09 and smaller than that of ZGGO:Cr^{3+} PLNPS powders (0.70). It can be explained that the contribution of surface Cr^{3+} in PLNPS to NIR luminescence is reduced due to the quenching effect of OH^- in HSA solution.

Furthermore, the NIR afterglow time of HSA aqueous dispersion of ZGGO:Cr^{3+} PLNPS annealed at 800 °C is obtained to be more than 1 h after 30-minute irradiation using 320 nm (Fig. 13). A phosphorescence spectrum is recorded at 60 min after stopping UV irradiation (inset, Fig. 13). NIR afterglow digital photos of HSA aqueous dispersion with different delay times are captured after stopping the irradiation for 15 min using 254 nm UV (images, Fig. 13). The above results suggest that ZGGO:Cr^{3+} PLNPS have potential applications for *in vivo* bio-imaging.

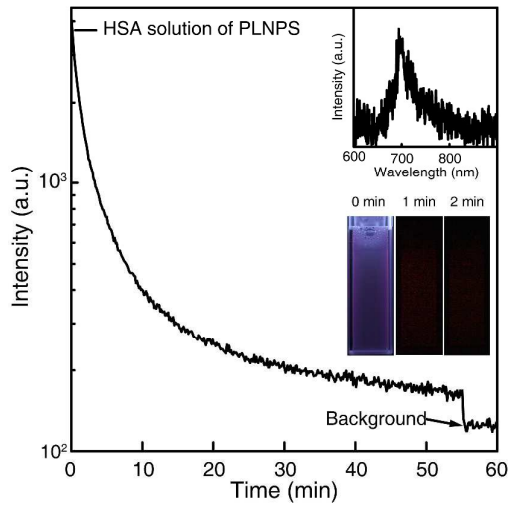

Fig. 13 NIR afterglow decay curve (monitored at 697 nm) of HSA aqueous dispersion of ZGGO:Cr^{3+} annealed at 800 °C (5 mg/mL) after 30-min irradiation with 320 nm UV light. The upper inset shows a phosphorescence spectrum recorded at 60 min after the irradiation stops. The bottom inset shows the NIR digital photos of HSA aqueous dispersion of ZGGO:Cr^{3+} annealed at 800 °C (5 mg/mL): the photos were recorded at 0, 1 and 2 min after the stoppage of the 15-minute 254 nm irradiation, respectively.

Conclusions

We have synthesized novel zinc gallogermanate PLNPS (~82 nm) using a one-step hydrothermal method. Subsequently, a vacuum-annealing strategy is adopted to improve NIR afterglow in the ZGGO:Cr^{3+} nanoparticles. For the optimized sample (annealed at 800 °C), the particle size shows no obvious change in comparison with the as-prepared sample. The persistent luminescence intensity increases by ~14 times and the afterglow time reaches to more than 15 h after the annealing. For the ZGGO:Cr^{3+} annealed at 880 and 950 °C, their persistent luminescence is enhanced but the nanoparticles show the aggregated-surface behavior. Upon 256 nm UV

excitation, there exist two dynamical processes: the energy transfer from host to Cr^{3+} and the direction excitation of Cr^{3+} through $^4A_2 \rightarrow {}^4T_1(^4P)$ transition and a stronger NIR persistent luminescence is observed relative to 320 and 440 nm excitation. After the vacuum annealing, there generates shallow and deep traps related to Zn_{Ga}'-Ga_{Zn}^{o} antisite defects and V_{Ge}-Cr^{3+}-V_O defect clusters, respectively. Finally, we apply ZGGO:Cr^{3+} PLNPS to HSA colloid solution and detect more than 1 h NIR persistent luminescence under 320 nm excitation. The quenching effect of NIR luminescence by OH^- in HSA solution is also observed based on the reduced contribution of surface Cr^{3+} in PLNPS to NIR luminescence. Our results suggest that ZGGO:Cr^{3+} PLNPS have potential applications for *in vivo* bio-imaging.

Acknowledgements

This work was supported by the National Natural Science Foundation of China (No. 11374047, No.11074031 and No. 11304036) and the financial assistance of China Scholarship Council.

References

1 W. Chen and J. Zhang, *J. Nanosci. Nanotechnol.*, 2006, **6**, 1159-1166.
2 Q. le Masne de Chermont, C. Chanéac, J. Seguin, F. Pelle, S. Maitrejean, J. P. Jolivet, D. Gourier, M. Bessodes and D. Scherman, *Proc. Natl. Acad. Sci. U. S. A.*, 2007, **104**, 9266-9271.
3 T. Maldiney, A. Lecointre, B. Viana, A. Bessière, M. Bessodes, D. Gourier, C. Richard and D. Scherman, *J. Am. Chem. Soc.*, 2011, **133**, 11810-11815.
4 Z. Pan, Y. Y. Lu and F. Liu, *Nat. Mater.*, 2012, **11**, 58-63.
5 F. Liu, W. Yan, Y. J. Chuang, Z. Zhen, J. Xie and Z. Pan, *Sci. Rep.*, 2013, **3**, 1554-1562.
6 T. Maldiney, A. Bessière, J. Seguin, E. Teston, S. K. Sharma, B. Viana, A. J. Bos, P. Dorenbos, M. Bessodes, D. Gourier, D. Scherman and C. Richard, *Nat. Mater.*, 2014, **13**, 418-426.
7 Z. Li, Y. Zhang, X. Wu, X. Wu, R. Maudgal, H. Zhang and G. Han, *Adv. Sci.*, 2015, DOI:10.1002/advs.201500001.
8 Z. Li, Y. Zhang, X. Wu, L. Huang, D. Li, W. Fan and G. Han, *J. Am. Chem. Soc.*, 2015, **137**, 5304-5307.
9 M. Allix, S. Chenu, E. Véron, T. Poumeyrol, E. A. Kouadri-, *Chem. Mater.*, 2013, **25**, 1600-1606.
10 A. Abdukayum, J. T. Chen, Q. Zhao and X. P. Yan, *J. Am. Chem. Soc.*, 2013, **135**, 14125-14133.
11 R. G. Burns, *Mineralogical applications of crystal field theory*, Cambridge University Press, Cambridge, U.K., 1993.
12 R. Shannon, *Acta Crystallogr., Sect. A: Found. Crystallogr.*, 1976, **32**, 751-767.
13 M. Imade, K. Murakami, D. Matsuo, H. Imabayashi, H. Takazawa, Y. Todoroki, A. Kitamoto, M. Maruyama, M. Yoshimura and Y. Mori, *Cryst. Growth Des.*, 2012, **12**, 3799-3805.
14 W. Mikenda and A. Preisinger, *J. Lumin.*, 1981, **26**, 53-66.
15 W. Mikenda and A. Preisinger, *J. Lumin.*, 1981, **26**, 67-83.
16 W. Mikenda, *J. Lumin.*, 1981, **26**, 85-98.
17 J. Derkosch and W. Mikenda, *J. Lumin.*, 1983, **28**, 431-441.
18 M. Grinberg, P. Macfarlane, B. Henderson and K. Holliday, *Phys. Rev. B: Condens. Matter*, 1995, **52**, 3917-3929.
19 W. Yan, F. Liu, Y.-Y. Lu, X.-J. Wang, M. Yin and Z. Pan, *Opt. Express*, 2010, **18**, 20215-20221.
20 Y. Tanabe and S. Sugano, *J. Phys. Soc. Jpn.*, 1954, **9**, 766-779.
21 M. Grinberg, *Opt. Mater.*, 2002, **19**, 37-45.
22 I. Nikolov, *Opt. Mater.*, 2004, **25**, 53-58.
23 M. Yamaga, P. I. Macfarlane, B. Henderson, K. Holliday, H. Takeuchi, T. Yosida and M. Fukui, *J. Phys.: Condens. Matter*, 1997, **9**, 569-578.
24 M. Grinberg, W. Jaskólski, P. I. Macfarlane and K. Holliday, *J. Phys.: Condens. Matter*, 1997, **9**, 2815-2829.
25 M. Grinberg and A. Mandelis, *Phys. Rev. B: Condens. Matter*, 1994, **49**, 12496-12506.
26 A. Bessière, S. K. Sharma, N. Basavaraju, K. R. Priolkar, L. Binet, B. Viana, A. J. J. Bos, T. Maldiney, C. Richard, D. Scherman and D. Gourier, *Chem. Mater.*, 2014, **26**, 1365-1373.
27 C. Liu, Z. Xia, M. S. Molokeev, Q. Liu and H. Guo, *J. Am. Ceram. Soc.*, 2015, **98**, 1870-1876.
28 R. Martin-Rodriguez, R. Valiente, F. Rodriguez and M. Bettinelli, *Nanotechnol.*, 2011, **22**, 265707-265713.
29 A. K. Parchur, A. I. Prasad, A. A. Ansari, S. B. Rai and R. S. Ningthoujam, *Dalton Trans.*, 2012, **41**, 11032-11045.
30 J. Zhao, Z. Lu, Y. Yin, C. McRae, J. A. Piper, J. M. Dawes, D. Jin and E. M. Goldys, *Nanoscale*, 2013, **5**, 944-952.
31 Q. Lu, F. Guo, S. Liang, A. Li and L. Zhao, J. Appl. Phys., 2008, **103**, 123533-123542.
32 S. S. Wang, W. T. Chen, Y. Li, J. Wang, H. S. Sheu and R. S. Liu, J. Am. Chem. Soc., 2013, **135**, 12504-12507.
33 A. Bessière, S. Jacquart, K. Priolkar, A. Lecointre, B. Viana and D. Gourier, *Opt. Express*, 2011, **19**, 10131-10137.
34 Y. Zhuang, J. Ueda and S. Tanabe, *Appl. Phys. Express*, 2013, **6**, 52602-52605.
35 N. Ibrahim, H. Ibrahim, S. Kim, J. P. Nallet and F. o. Nepveu, *Biomacromolecules*, 2010, **11**, 3341-3351.
36 S. V. Eliseeva and J. C. G. Bünzli, *Chem. Soc. Rev.*, 2010, **39**, 189-227.
37 D. Yuan, M. C. Tan, R. E. Riman and G. M. Chow, *J. Phys. Chem. C*, 2013, **117**, 13297-13304.
38 W. Yu, W. Xu, H. Song and S. Zhang, *Dalton Trans.*, 2014, **43**, 6139-6147.

Graphical and textual abstract for the Table of Contents

Novel Cr^{3+} doped ZGGO nanoparticles with 697 nm near-infrared super long afterglow were prepared by hydrothermal method and a subsequent vacuum-annealing strategy.